PHYSICAL REVIEW B **96**, 195304 (2017)

Structure and evolution of semiconducting buffer graphene grown on SiC(0001)

M. Conrad,[1] J. Rault,[2] Y. Utsumi,[2] Y. Garreau,[2,3] A. Vlad,[2] A. Coati,[2] J.-P. Rueff,[2] P. F. Miceli,[4] and E. H. Conrad[1,*]
[1]*Georgia Institute of Technology, Atlanta, Georgia 30332-0430, USA*
[2]*Synchrotron SOLEIL, L'Orme des Merisiers, Saint-Aubin, 91192 Gif sur Yvette, France*
[3]*Université Paris Diderot, Sorbonne-Paris-Cité, MPQ, UMR 7162 CNRS, Bâtiment Condorcet, Case 7021, 75205 Paris Cedex 13, France*
[4]*Department of Physics and Astronomy, University of Missouri, Columbia, Missouri 65211, USA*

(Received 7 July 2017; revised manuscript received 29 August 2017; published 13 November 2017)

Using highly controlled coverages of graphene on SiC(0001), we have studied the structure of the first graphene layer that grows on the SiC interface. This layer, known as the buffer layer, is semiconducting. Using x-ray reflectivity and x-ray standing wave analysis, we have performed a comparative study of the buffer layer structure with and without an additional monolayer graphene layer above it. We show that no more than 26% of the buffer carbon is covalently bonded to Si in the SiC interface. We also show that the top SiC bilayer is Si depleted and is likely the cause of the incommensuration previously observed in this system. When a monolayer graphene layer forms above the buffer, the buffer layer becomes less corrugated with signs of a change in the bonding geometry with the SiC interface. At the same time, the entire SiC interface becomes more disordered, presumably due to entropy associated with the higher growth temperature.

DOI: 10.1103/PhysRevB.96.195304

I. INTRODUCTION

The first graphene "buffer" layer that grows on the SiC(0001) surface is one of the most important examples of functionalized graphene. It is normally in a semiconducting state due to self-functionalization caused by sp^3 bonding to silicon atoms in the SiC interface [1,2]. The buffer's band gap can be increased by additional functionalization with fluorine [3] or transformed to a metallic graphene form by H_2 intercalation that breaks the sp^3 bonding to the interface Si [4]. In fact numerous studies have shown that the buffer graphene's electronic properties can be altered by changing the interfacial Si bonds [2–9], implying that the buffer's electronic properties can in principle be modified in a controlled fashion. However, the level of understanding necessary to systematically alter the buffer's properties has remained elusive because structural details, such as the number of C-Si bonds and their geometry, are simply not well understood.

The bonding geometry problem is underscored by the number of different states calculations predict for the buffer. *Ab initio* calculations using a $(\sqrt{3}\times\sqrt{3})_{\mathrm{SiC}}R30^\circ$ cell find a wide band gap buffer while calculations on the larger, experimentally observed $(6\sqrt{3}\times6\sqrt{3})_{\mathrm{SiC}}R30^\circ$ cells [10,11] find metallic states running through the Fermi energy (E_F) [5–7]. The applicability of these early calculations is problematic because they all assumed that the SiC surface is bulk terminated [7,8,12], an assumption that we now know is incorrect. Recent x-ray diffraction studies have demonstrated that the buffer-SiC interface is not commensurate with SiC [9]. Instead, the system has an incommensurate (IC) modulation period $\lambda = 6(1+\delta)a_{\mathrm{SiC}}$ ($\delta = 0.037$) that is close to the $(6\times6)_{\mathrm{SiC}}$ subcell of the $(6\sqrt{3}\times6\sqrt{3})_{\mathrm{SiC}}R30^\circ$ cell. Tight-binding (TB) calculations, using an IC in-plane distortion of a bulk-terminated surface, show that the distortion can open a band gap similar to that measured by angle-resolved photoemission spectroscopy (ARPES) [2,9]. However, before more sophisticated *ab initio* calculations on the IC structure can be attempted, some details of the interface structure will be needed to limit the parameter space for these taxing computations.

Experimentally determining the buffer's structure is also problematic. The first experimental structural studies were done on samples grown in ultrahigh vacuum (UHV) [13]. These samples suffered from both reduced long-range order [14–16] and poor control of both the number of graphene layers and their lateral distribution [14,17]. Sample uniformity turns out to be extremely important because both the electronic and structural properties of the buffer are now known to change when monolayer (ML) graphene grows above the buffer [9]. This means that measured structures on nonuniform films represent some unknown average of two different structures.

In this work, we use x-ray standing wave (XSW) and x-ray reflectivity (XRR) measurements to study two types of buffer graphene films grown on SiC(0001): a buffer-only film ($\mathrm{BG_o}$) and a buffer graphene film ($\mathrm{BG_{ML}}$) that has a monolayer graphene layer grown above it. Because of the improved thickness control and the layer uniformity achievable in silicon sublimation controlled RF furnace grown graphene, we are able to discriminate structural changes in these two different types of buffer graphene. We show that the buffer structure and the bonding to the SiC are very different with and without a monolayer graphene layer grown above the buffer layer. While these differences help explain recent in-plane x-ray diffraction results [9], they complicate previous XSW analysis that used multilayer films [18]. As we will show, the mixed coverage films led to a misidentification of the buffer-SiC bonding component in the buffer's C 1s spectrum. We also show that the buffer-only film has a large vertical corrugation and that its close distance to the substrate indicates a strong sp^3 C-Si bond. The buffer's C-Si bond length increases and the corrugation amplitude becomes smaller when the ML grows above the buffer, indicating a change in the distribution of graphene-Si bonds to the SiC interface. Finally, we confirm that the Si concentration in the last Si-C bilayer (see Fig. 1) is reduced as previously reported [18]. Rather than being a growth artifact as

---

[*] edward.conrad@physics.gatech.edu

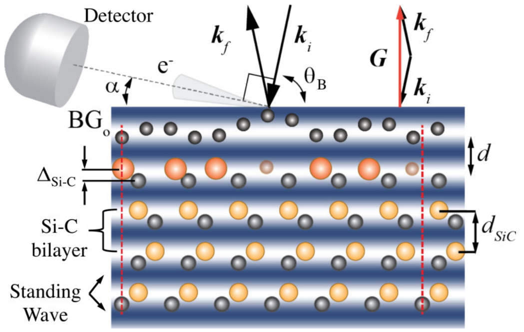

FIG. 1. Schematic of the XSW geometry on the SiC(0001) surface. Gray circles show the buckled BG_o buffer layer above the top SiC bilayer (yellow and gray circles are Si and C, respectively, in the SiC lattice). The photoelectrons are measured by the detector at a takeoff angle α. The standing-wave period, d, is shown using the $G = 2\pi/d_{\rm SiC}$ Bragg reflection.

previously conjectured, we show that Si vacancy concentration is an equilibrium structure of the top SiC bilayer. We find 25% SiC vacancies in the top SiC bilayer (compared to the bulk value) for both BG_o and BG_{ML} films. This result helps put an upper limit of 26% on the number of buffer-carbon atoms bonded to silicon at the interface. The reduced Si concentration is coupled with a vertical compression in the Si-C bilayer below the buffer, suggesting that the Si vacancy concentration may help drive the incommensurate structure of the BG_o and SiC interface.

II. EXPERIMENTAL METHODS

A. Sample preparation

The substrates used in these studies were n-doped, chemical-mechanical planarization polished (CMP), on-axis 4H-SiC(0001). The graphene was grown in a confinement-controlled silicon sublimation furnace (CCS) [19]. In the CCS method, graphene growth is a function of temperature, time, and crucible geometry that sets the silicon vapor pressure. With the current crucible design [20], a single semiconducting BG_o graphene layer grows at a temperature of 1400 °C after 30 min. Heating at 1560 °C for 20 min causes the BG_o layer to transform into a graphene ML as a new BG_{ML} buffer layer forms below the ML. Prior to XSW and XRR experiments, the BG_o and BG_{ML}+ML samples were characterized by x-ray photoemission spectroscopy (XPS) and Raman to determine film quality and ML coverage.

Figure 2 compares the Raman spectra of the BG_o film to the spectra from a BG_{ML}+ML film. The BG_o film spectrum lacks the ML 2D and sharp G peaks but shows two additional features; a B_o peak at 1480 cm^{-1} and a broad G+D peak between 2900 and 3100 cm^{-1}. The latter two features are known to be associated with a pure buffer film [21,22]. Using the ML 2D intensity as a reference and the background noise as an upper limit on the buffer 2D peak, we estimate that the ML coverage must be less than <3%. This is consistent with ARPES estimates of the ML coverage in a BG_o film [2]. The majority of the ML coverage is expected to be associated with a ML that nucleates at intrinsic step edges [23]. The Raman spectrum was measured at three positions (each 3 mm apart) on the sample and no significant changes in the Raman were found, indicating the large-scale film uniformity necessary for XRR experiments.

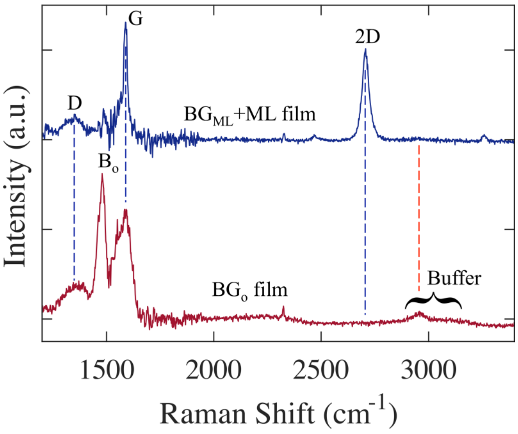

FIG. 2. A comparison of the Raman spectra from a buffer-only film and a ML graphene film grown on SiC(0001). A bulk SiC spectrum has been subtracted from each spectra. The ML film shows the D, G, and 2D peaks associated with graphene on SiC(0001) [24]. The BG_o film lacks the 2D and sharp G peaks but has two characteristic features: the B_o peak at 1480 cm^{-1} and a broad "buffer" spectrum between 2900 and 3100 cm^{-1}. The ML coverage in the BG_o film is less than 3%.

B. XSW and XRR methods

XRR measurements were conducted at room temperature in ultrahigh vacuum (UHV) at the SIXS beamline at the Synchrotron SOLEIL using a photon energy of $E = 12.8$ keV. Prior to x-ray exposure, the samples were heated to 500 °C in UHV to remove absorbed contaminants. The momentum transfer vector, $\mathbf{K}$, is defined as $\mathbf{K} = \mathbf{k}_f - \mathbf{k}_i$ where $\mathbf{k}_i$ and $\mathbf{k}_f$ are the momenta of the incident and reflected x-ray beams, respectively. For the elastic scattering considered here, $|k_f| = |k_i| = E/\hbar c$. $\mathbf{K} = (h,k,l)$ represents a point in reciprocal space that is written in terms of the bulk hexagonal coordinates of SiC: $\mathbf{K} = h\mathbf{a}^*_{\rm SiC} + k\mathbf{b}^*_{\rm SiC} + l\mathbf{c}^*_{\rm SiC}$ where $|\mathbf{a}^*_{\rm SiC}| = |\mathbf{b}^*_{\rm SiC}| = 4\pi/(a_{\rm SiC}\sqrt{3}) = 2.3556$ Å^{-1} and $|\mathbf{c}^*_{\rm SiC}| = 2\pi/c_{\rm SiC} = 0.6233$ Å^{-1}. The XRR polarization and geometric corrections were performed to allow comparison between the measured reflectivity intensities and calculated intensities from the model discussed in Sec. III C [25].

In the XSW experiment, the sample is oriented so that the incoming x-ray beam of energy E_B satisfies the condition that $\mathbf{K} = \mathbf{G}$, where $\mathbf{G}$ is a reciprocal lattice vector of SiC (i.e., a Bragg reflection). This geometry produces a standing wave whose crests are $\lambda/2 = d = 2\pi/|\mathbf{G}|$ apart and perpendicular to $\mathbf{G}$ (see Fig. 1). By changing the incident photon energy relative to E_B, the standing wave will move in the $\mathbf{G}$ direction exciting photoelectrons as a wave maximum passes through a plane of atoms (see Fig. 1) [26,27]. The photoelectron intensity for a particular element j in the material, $I^G_j(E)$, will therefore be a function of E and thus related to the vertical position of that element.

The XSW experiments were carried out at the GALAXIES beamline on the Synchrotron SOLEIL [28]. We used the $\mathbf{G} = (004)$ Bragg reflection to produce the standing wave with $d = 2.52$ Å. The Bragg angle for the (004) reflection was $\theta_B \sim 78^\circ$ corresponding to an incident photon energy of $E_B = 2512$ eV. All measurements were done at room temperature with an overall energy resolution ∼300 meV. Recoil effects are estimated to increase the broadening to ∼400 meV [29]. We place an upper limit on the total XPS resolution to be 0.45 eV based on the measured ML graphene C 1*s* linewidth (see Supplemental Material [30] for the estimate of the XPS resolution that contains Ref. [31]). The takeoff angle, α, for the photoelectron detector was 10° to improve surface sensitivity in the XPS spectra.

For the studies presented in this work, we are interested in the photoelectron yield from the C 1*s* core levels that have components from both the carbon in SiC and the carbon in the buffer layer. The details of analyzing the C 1*s* spectra as a function of both photon energy $E - E_B$ and binding energy BE require some care. We do this by first setting the number of components in the spectrum (see Sec. III A) and then fitting each spectrum $I_E(\mathrm{BE})$ for a range of photon energies around E_B. The fitting is done by minimizing the global χ_g^2 (see Supplemental Material [30]). The global χ_g^2 is the χ^2 for a single C 1*s* spectrum fit, at a single photon energy, summed over fits for every incident photon energy in the data set. While each component's line shape parameters, i.e., width and position, are allowed to vary, they are constrained to be independent of the incident photon energy. Only the components' areas are allowed to vary as a function of E. A Shirley background has been subtracted from every core-level spectrum. We use a Doniach-Sunjic line shape for the graphene peak and a Voigt line shape for the buffer carbon, bulk carbon component, and Si 2*s* core levels.

III. RESULTS

While XRR is able to study surfaces with buried interfaces, the phase problem makes structural measurements difficult. Emery *et al.* [18] have shown how combining XSW and XRR studies of the SiC-graphene interface can help overcome the phase problem. However, in the particular case of the buffer layer, XSW analysis has its own problems that were not recognized and that we now discuss before presenting our experimental results.

The C 1*s* XPS spectra of graphene grown on SiC(0001) was thought to contain four components: S_1, S_2, S_{ML}, and C_B. S_1 and S_2 are from the buffer carbon layer that contains C-Si bonds to the interface and distorted C bonds in the unbonded part of the buffer layer. The S_{ML} component is from sp^2 C-C bonds in any graphene that grows above the buffer. The C_B component is from sp^3 C-Si bonds in bulk SiC [1]. However, several theoretical calculations along with experimental scanning transmission electron microscopy (STEM) and x-ray diffraction measurements show an incommensurate structure that suggests reduced interfacial bonding. All these works indicate that part of the buffer should also have sp^2-bonded carbon [7,9,32]. This possibility is shown schematically in Fig. 3 and implies that at least one additional component (which we we label S_G) may be present in the buffer's C 1*s* spectrum. Any partial ML film would have an S_{ML} component obscuring any possible sp^2-bonded carbon in the buffer layer's C 1*s* spectrum. Furthermore, any substantial reconstruction of the top SiC bilayer could also cause new components to arise in the C 1*s* spectrum near the BE of the bulk C_B component. It will therefore be important in our subsequent XPS analysis to explore how additional C 1*s* peaks affect the XSW results.

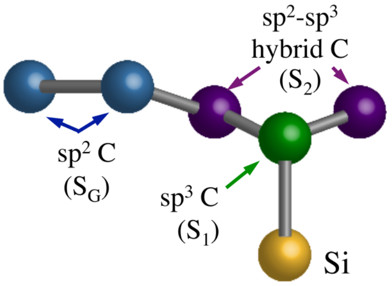

FIG. 3. Schematic model of the transition from sp^3 buffer carbon bonded to silicon in the SiC interface to sp^2 graphitic carbon through a hybrid carbon back bond. S_1, S_2, and S_G refer to the three C 1*s* XPS components described in Sec. III.

The large ML coverages in samples used in earlier studies cause an additional and more important problem. If the BG_o and BG_{ML} layers were structurally identical, the ML coverage would only complicate the spectral analysis of the C 1*s* spectrum. We now know that this assumption is wrong and that there are substantial changes in the buffer's structure when a ML grows above it [9]. This means that a substantial ML coverage will cause both the XSW and XRR data to give results that represent an unknown weighted average of two different structures making it impossible to determine a unique BG_o structure. For XRR, the ML coverage has a further complication. Because both the BG_o and BG_{ML} layer distributions are broad in Z while ML or bilayer graphene layers are narrow [12,18], the buffer's contribution to the scattered amplitude will be smaller than the ML's [33]. This effect is demonstrated by comparing the calculated XRR reflectivity of a bulk-terminated SiC surface to the measured buffer or ML films (see Fig. 4). Between Bragg peaks ($l = 0$, 4, and 8), the buffer layer causes small changes (about a factor of 4–10) with respect to the bulk-terminated surface. A ML film on the other hand can produce changes that are a factor of 10 larger and thus obscure reflectivity contributions from the buffer film [see Fig. 4(b)].

The problems associated with ML films we identified above are the reasons we use samples with high coverage control. Our XSW studies will consider the possibility of new components in the C 1*s* fits. Recognizing the possible systematic errors associated with multiple peak fits in the C 1*s* spectra, we will use the XSW-derived Z distributions as starting parameters for XRR reflectivity fits. These distributions will be allowed to vary (with restrictions) to refine the BG_o and BG_{ML} layer structures.

A. Fitting the XPS spectra

Figure 5(a) shows a 3-component fit (S_1, S_2, and C_B used in previous studies) to the BG_o layer when no ML graphene is expected on the sample. It must be emphasized that the

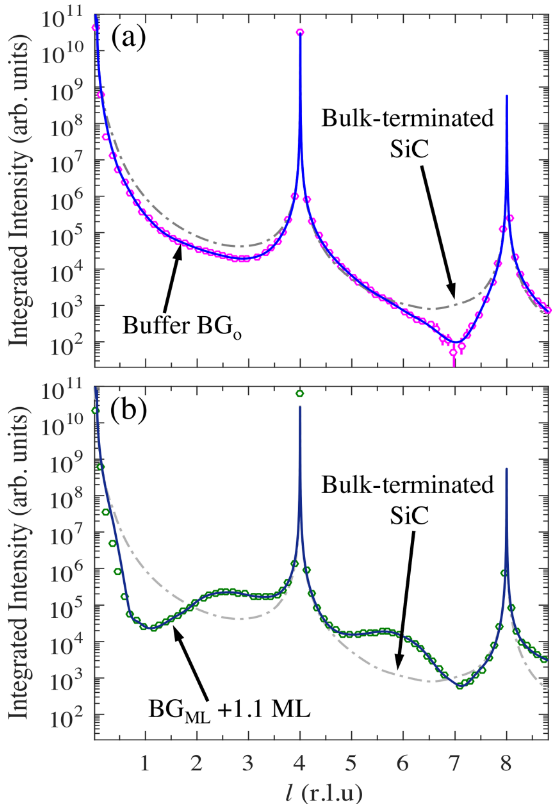

FIG. 4. The experimental x-ray reflectivity (open circles) of (a) a BG_o-only film, and (b) a ML film above the BG_{ML} layer. For the BG_o film, the calculated reflectivity (solid lines) in (a) uses a buffer composed of three components (S_1, S_2, and S_G) plus a small 1% ML coverage. Details of the calculation are given in Sec. III C. For the ML film in (b), the calculation uses a single S_1 component buffer for the BG_{ML} layer. For comparison, the calculated reflectivity from a bulk-terminated surface (dashed lines) is shown in both plots.

relative areas of the individual components in Fig. 5 are not a measure of their relative concentrations as will be discussed in Sec. III B. In fact the photon energy used for the C 1*s* spectra shown in Fig. 5 was deliberately chosen to minimize the S_1 component that can obscure any components that occur in an energy range where a graphene ML component would appear. Our 3-component fit is very similar to those found in the work of Emtsev *et al.* [1]. In that earlier work, the C 1*s* spectrum was monitored as a function of growth, so we would expect very little ML coverage in their early growth spectra, explaining the similarity of their fit to ours.

While 3 components can fit the C 1*s* spectrum, there are large residuals [see Fig. 5(d)] suggesting that other peaks could be present. As discussed above and shown in Fig. 3, we expect the BG_o layer to have a structure that could have an additional C 1*s* component. However, if we add a fourth component near the BE of ML graphene (285.5 eV), the fitting procedure moves the peak to a position close to the bulk C_B position. Because of its proximity to C_B, we label the new peak C'_B [see Fig. 5(b)]. It is certainly reasonable that the top SiC bilayer would relax as some bilayer Si bonds to the buffer and distorts the bilayer Si-C bonds. This would strain the top SiC bilayer from the bulk configuration and lead to a range of binding geometries that would broaden the C_B peak and possibly give rise to a C'_B component. The overall effect on the C 1*s* fit using the C'_B component is very dramatic. The intensity ratio of S_1 to S_2 reverses and both peaks become narrower as S_1 moves to higher BE. Note that despite these changes, the residual map is only slightly improved [see Figs. 5(e)].

The residual map for the BG_o film can be substantially improved by adding a fifth component [see Figs. 5(c) and 5(f)]. The best-fit position of the new peak is labeled S_G because its BE is near that of graphite, between the BE of the buffer peaks and the bulk carbon peaks. The S_G peak causes S_1 to move to even higher BE and further increase the intensity ratio of S_1 to S_2. In fact, the spectral ratio of S_1 to S_2 in the 5-component fits resembles that found by Emery *et al.* [18] using a ML film. The similarity between our 5-component fit and Emery *et al.* [18] might be expected given that the S_G peak influences the fit shape in much the same way as a true ML graphene peak would. The peak positions and widths of the different component fits for the BG_o C 1*s* spectra are summarized in Table I. As we will show in Sec. III B, the three different C 1*s* decompositions lead to very different BG_o layer structures.

There are also multiple ways to fit the ML film's C 1*s* spectra. Figures 5(g) and 5(h) show fits for a BG_{ML}+ML film using different numbers of C 1*s* components. The 3-component fit [Fig. 5(g)] gives a reasonable fit to the ML C 1*s* spectrum. Note that we label the higher binding energy peak as S_1 not S_2. This is because its BE lies closer to S_1 in the BG_o 4- and 5-component fits. As we will show in Sec. III B, the assignment of the highest BE peak to S_1 will be supported by the XSW results. Adding a fourth component to the ML spectrum significantly improves the residuals [see Fig. 5(j)] but has remarkably little affect on the parameters for the S_1 component. We label the additional peak S'_{ML} because no matter what the initial guess for its BE is, the best-fit BE is very near the S_{ML} monolayer peak's BE. Adding a fifth component to the ML film fit does not give a statistically significant fit and will not be discussed further (see Supplemental Material [30]).

As is clear from the discussions above, fitting the C 1*s* spectra is difficult because the components are very broad (compared to instrument resolution) and close together in binding energy. While statistically it is possible to identify the 5-component BG_o as better than fits using fewer components, it is not clear whether the 5-component fit represents the physical description of the buffer layer. Identifying the best representation of the actual BG_o structure will require comparison of both XSW and XRR analysis to form a self-consistent model of the buffer layer.

B. X-ray standing waves

The normalized photoelectron yield $Y_j^G(E)$ for element j in an XSW experiment is given by [26,27,34]

$$Y_j^G(E) = 1 + R^G(E) + 2\sqrt{R^G(E)} \times \int_{\text{vol}} \rho'_j(r) \cos\left[\nu(E) - 2\pi P_j^G\right] dr. \tag{1}$$

$R^G(E)$ is the energy-dependent x-ray reflectivity at the Bragg point [$G = (004)$ in this work] and $\nu(E)$ is the phase of

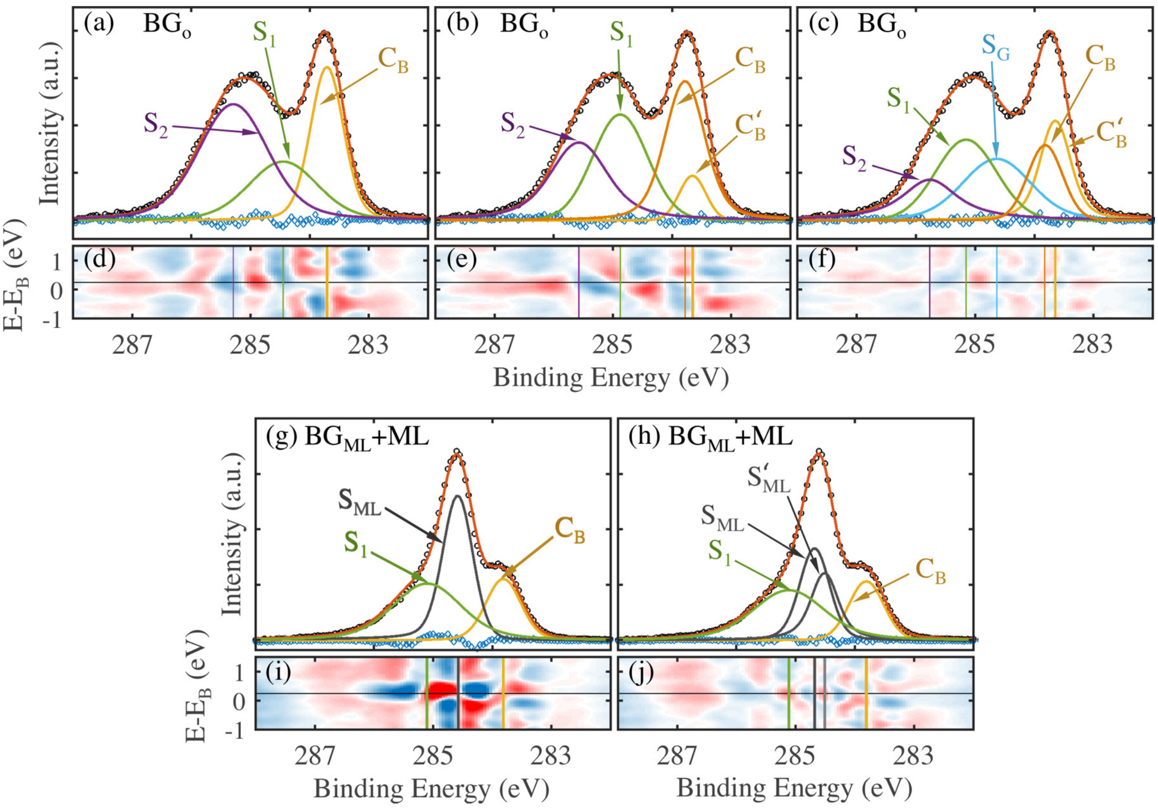

FIG. 5. The C 1s spectral decomposition for a BG$_o$ film [(a), (b), and (c)] and a BG$_{ML}$+ML film [(g) and (h)]. The fits are at a photon energy of $E - E_B = 0.25$ eV. The residual maps [(d), (e), (f), (i), and (j)] for each fit are shown as a function of $E - E_B$ and binding energy. Vertical lines in the maps mark the best-fit BE peak positions of each component. (a) A buffer-only C 1s spectra using a 3-component fit with two buffer components, S$_1$ and S$_2$, plus a bulk SiC component C$_B$. (b) A 4-component fit similar to (a) but with an additional component labeled C$'_B$. (c) A 5-component fit similar to (b) but with the additional component S$_G$. (g) A BG$_{ML}$+ML film C 1s spectra using a 3-component fit with an S$_1$ buffer component, a ML component S$_{ML}$, and a bulk SiC component C$_B$. (h) A 4-component fit similar to (g) but with an additional component labeled S$'_{ML}$.

the standing wave (see Supplemental Material [30] for a description of the calculation of $\nu(E)$ and $R^G(E)$ that contains Refs. [35–37]) [26]. Both are calculated from the bulk crystal structure [38]. $\rho'_j(r)$ is the density distribution of the jth element and $P^G_j = \mathbf{G}\cdot\mathbf{r_j}/(2\pi)$ (where r_j is the position of the jth atom, modulo d). Rather than deal with arbitrary atom distributions, we will only consider atoms vertically distributed in discrete planes at positions z_j in a Gaussian distribution. This is done by writing $\rho'_j(r)$ as a convolution of a delta function with a normalized Gaussian distribution whose width is $\sigma_{z,j}$. This reduces Eq. (1) to

$$Y^G_j(E) = 1 + R^G(E) + 2\sqrt{R^G(E)}f_j \cos\left[\nu(E) - 2\pi P^G_j\right], \tag{2a}$$

$$f_j = e^{-\sigma^2_{z,j}G^2/2}. \tag{2b}$$

$Y^G_j(E)$ is related to the experimental intensity by a normalizing constant: $I^G_j(E) = N_j Y^G_j(E)$. Neglecting photoelectron attenuation (a reasonable assumption for the buffer-only film)

TABLE I. The fitted C 1s BE positions and FWHM (FW$_j$) for both buffer-only and buffer+ML films. BE is given as shifts, ΔE_j, relative to the bulk carbon BE at 283.7 eV. All values are in eV and the statistical uncertainty is 0.1 eV. The statistically significant best-fit spectra are highlighted with italics: the 5-component and 4-component fits for the buffer-only and ML films, respectively.

		ΔE_{S2}	FW$_{S2}$	ΔE_{S1}	FW$_{S1}$	ΔE_{SG}	FW$_{SG}$	ΔE_{CB}	FW$_{CB}$	$\Delta E_{CB'}$	FW$_{CB'}$
Buffer	3-Comp	1.58	1.38	0.74	1.38			0.0	0.66		
	4-Comp	1.92	1.15	1.23	1.07			0.0	0.53	0.1	0.8
	5-Comp	2.12	1.12	1.51	1.21	0.99	1.37	−0.1	0.61	0.18	0.69
		ΔE_{S1}	FW$_{S1}$	ΔE_{ML}	FW$_{ML}$	$\Delta E_{ML'}$	FW$_{ML'}$	ΔE_{CB}	FW$_{CB}$		
ML	3-Comp	1.35	1.37	0.77	0.57			0.1	0.70		
	4-Comp	1.31	1.44	0.87	0.56	0.70	0.44	0.1	0.69		

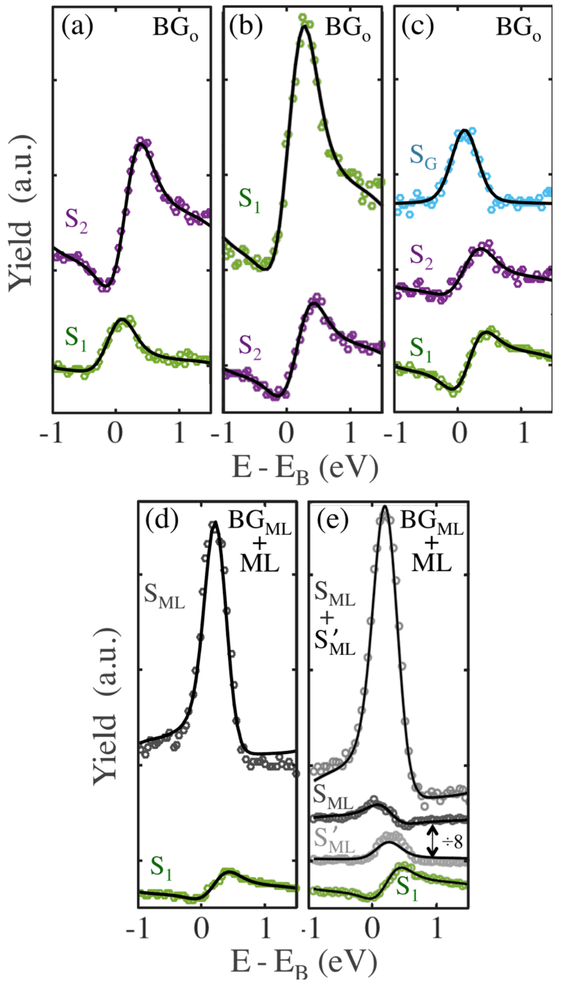

FIG. 6. (a), (b), and (c) show XSW yield data (○) for the BG$_\text{o}$ film using 3-, 4-, and 5-component fits for the C 1s spectra, respectively. Solid lines are fits using Eq. (2a). (d) and (e) show yield data and fits for a BG$_\text{ML}$+ML film derived from a 3- and 4-component C 1s fit, respectively. In (e) we also show the intensity and yield from the sum of S$_\text{ML}$ and S$'_\text{ML}$ peaks.

the coverage of a given C 1s component is then related to the N_j's: $\theta_j \sim N_j/\Sigma N_j$.

Figures 6(a), 6(b) and 6(c) show the experimental yields for the BG$_\text{o}$ film derived from 3-, 4-, and 5-component C 1s fits. The fits for the ML film, using 3 and 4 C 1s components, are shown in Figs. 6(d) and 6(e). We point out that while 4 components (S$_1$, S$_\text{ML}$, S$'_\text{ML}$, and C$_\text{B}$) give the best ML XPS fit, there is significant ambiguity in assigning Z positions to the S$_\text{ML}$ and S$'_\text{ML}$ peaks because of the modulo 2.52 Å in the phase P_j in Eq. (2a). This is partly due to the existence of a partial bilayer graphene layer (see Sec. III C below). The result of the phase problem is that we have two options for assigning the structure derived from the S$_\text{ML}$ peak and the S$'_\text{ML}$ peak. Either they represent something like an S$_2$ component in the BG$_\text{ML}$ layer and a ML component above or they represent the ML above the BG$_\text{ML}$ layer and a bilayer above the ML (see the Supplemental Material [30]). This ambiguity again points out the difficulty in determining the buffer structure when a significant ML film is present. We have also fitted the summed intensity S$_\text{ML}$ + S$'_\text{ML}$ to give an averaged ML position that is shown in Fig. 6(e) and given in Table II. Details of the fits, including the bulk carbon and silicon XSW analysis, are given in the Supplemental Material [30]. All of the XSW fit parameters are given in Tables II and III.

While all the BG$_\text{o}$ yield fits are very good, regardless of the number of components in the spectral decomposition, there are major differences in their Z distributions. What is remarkable about the fits is that no matter how many components are used in the C 1s spectra, the fits to the yield curves are essentially equally good. To make comparisons between the different fits easier to visualize, we have plotted their different Z distributions in Fig. 7. For reference, we have marked the 1.9 Å C-Si bond distance between buffer carbon and interfacial silicon measured by STEM in Fig. 7 [32]. Note that the STEM value is close to the 1.89 Å bulk SiC bond length.

There are a number of observations from the XSW results that indicate that the 5-component fit is closer to the actual BG$_\text{o}$ distribution. First, the 3- and 4-component fits give a

TABLE II. XSW results for the BG$_\text{o}$ and BG$_\text{ML}$+ML films. Results are shown for 3-, 4-, and 5-component fits to the BG$_\text{o}$ film and 3- and 4-component fits to the BG$_\text{ML}$+ML. The parameters for the 4-component ML film only include results where the S$_\text{ML}$ and S$'_\text{ML}$ C 1s intensities are summed for the yield fit. The Z positions are shown relative to the position of the last Si layer. Note that $(Z - Z_\text{Si})$ for S$_1$ and S$_2$ for the 5-component fit are in italics to highlight that their z distance is inverted.

		P	$(Z - Z_\text{Si})$[a] (Å)	f	σ (Å)	θ
BG$_\text{o}$	S$_2$	−0.02(2)	2.37(4)	0.52(4)	0.46(2)	0.70(1)
(3-peak)	S$_1$	1.23(5)	3.01(1)	0.3(4)	0.6(1)	0.30(1)
BG$_\text{o}$	S$_2$	−0.04(1)	2.33(4)	0.56(5)	0.43(3)	0.24(1)
(4-peak)	S$_1$	0.07(3)	2.61(7)	0.36(4)	0.58(3)	0.76(2)
BG$_\text{o}$	S$_2$	−0.03(5)	*2.5(1)*	0.48(9)	0.48(7)	0.32(1)
(5-peak)	S$_1$	−0.07(1)	*2.26(3)*	0.67(5)	0.36(4)	0.31(1)
	S$_\text{G}$	0.28(2)	3.13(6)	0.7(2)	0.3(1)	0.36(2)
BG$_\text{ML}$	S$_1$	−0.01(1)	2.39(3)	0.47(4)	0.49(3)	
(3-peak)	S$_\text{ML}$	−0.72(1)	5.64(2)	0.97(6)	0.09(8)	
BG$_\text{ML}$	S$_1$	−0.06(2)	2.28(5)	0.44(4)	0.51(3)	
(4-peak)	S$_\text{ML}$ +S$'_\text{ML}$	0.27(2)	5.63(5)	1.0(1)	0.0(1)	

[a] The position of the Si layer is determined by the XSW yield fits to the Si 2s core level; $Z_\text{Si} = 0.09$ Å (see Table III).

TABLE III. XSW results for bulk carbon C 1s and bulk silicon Si 2s. We have also summed the C$_\text{B}$ and C$'_\text{B}$ C 1s intensities for the 5-component BG$_\text{o}$ film before the yield fitting.

		P_j	Z_j (Å)	f_j	σ_j (Å)
BG$_\text{o}$	C$_\text{B}$	−0.26(5)	1.80(6)	0.78(8)	0.3(1)
	C$'_\text{B}$	−0.20(5)	1.92(6)	0.78(8)	0.3(1)
	C$_\text{B}$+C$'_\text{B}$	−0.24(1)	1.87(2)	0.79(5)	0.27(4)
	Si$_\text{B}$	0.04(1)	0.09(2)	1.00(3)	0.05(4)
BG$_\text{ML}$	C$_\text{B}$	−0.25(1)	1.89(2)	0.72(5)	0.33(2)
	Si$_\text{B}$	0.04(1)	0.09(2)	0.99(3)	0.07(4)

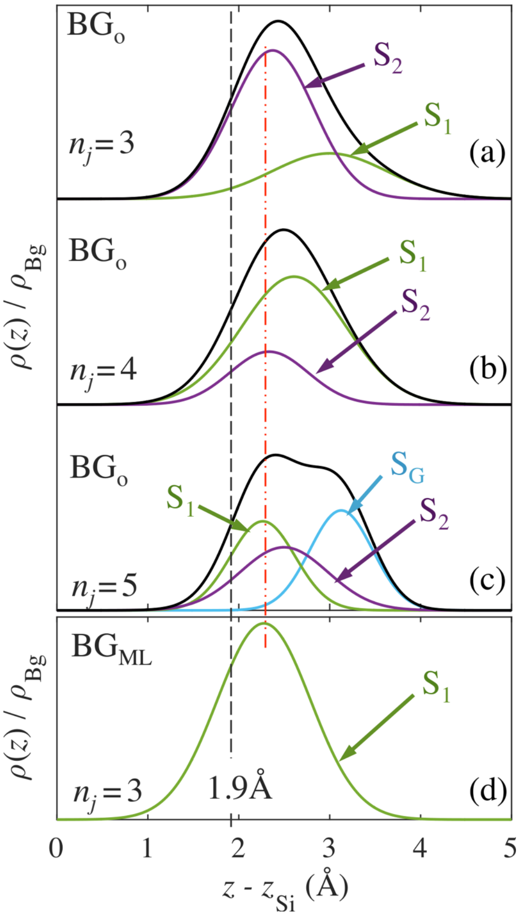

FIG. 7. Comparison of the XSW-derived vertical density distributions, $\rho(z)$, of the BG$_o$ and BG$_{ML}$+ML films relative to the last Si layer in the SiC(0001) surface (located at Z_{Si}). $\rho(z)$ is normalized to the BG$_o$ density. (a), (b), and (c) are for the BG$_o$ film using 3-, 4-, and 5-component fits, respectively. (d) is the profile of the BG$_{ML}$ layer using 4 components where the S$_{ML}$ and S$'_{ML}$ intensities have been summed. The red vertical dash-dotted line marks the S$_1$ position in the BG$_o$ film in (c). The black vertical dashed line marks the distance between buffer-carbon and Si measured by STEM [32].

BG$_o$ distribution that is essentially a broad Gaussian with the S$_2$ component closer to the SiC interface [Figs. 7(a) and 7(b)]. The essentially Gaussian shape is *inconsistent* with experimental STEM profiles of the buffer that indicate a sharper Z distribution [32]. In fact the 3-component fit finds that the S$_2$ atoms closer to the SiC are more than twice as numerous as the S$_1$ atoms farther away (see Table II). This contradicts both STEM results and theory predictions that the bonded carbon (presumably S$_2$ in the 3- and 4-component fits) is a much smaller fraction of the buffer carbon. Finally, both the 3- and 4-component fits find the unphysical result that 23% of the buffer carbon lies closer to Si than the smallest known C-Si bond distance of 1.89 Å.

There is one more result that points to the 5-component C 1s fit being the correct deconvolution of the BG$_o$ XPS spectrum. As already noted, XSW analysis predicts that the S$_2$ component from 3- and 4-component fits to the C 1s XPS spectra is associated with buffer carbon closest to the last bulk Si layer. This was the same result found in XSW experiments by Emery *et al.* [18] using a ML sample. However, our 5-component XSW analysis shows just the opposite result. Using the 5-component fit, we find that S$_1$ is closest to the Si layer indicating that S$_1$, not S$_2$, is from buffer carbon bonded to silicon. The proposal that S$_1$ is closest to the Si layer was first made by Emtsev *et al.* [1] in XPS studies on a series of samples ranging from no graphene to several monolayers. They noted that the buffer's σ bands were downshifted by 1.0 eV compared to graphite. The shift meant that the S$_1$ and S$_2$ buffer carbon peaks were also shifted to high BE relative to neutral graphite. Since the sp^2-bonded carbon must be at a higher BE than C-Si bonds, they concluded that the S$_1$ feature must be associated with buffer-Si bonds.

The Emtsev interpretation that S$_1$ is closer to the SiC is further supported by comparing our ML and buffer layer results. We can fit the ML film C 1s spectra two ways with the BG$_{ML}$ layer component that we labeled S$_1$ in Figs. 5(g) and 5(h). We can either use the 3-component fit with the S$_{ML}$, C$_B$, and S$_1$ or equally well using the 4-component fit. Since the BG$_{ML}$ S$_1$ component is the only component close to the interface in the ML film, it must have a considerable fraction of carbon bonded to Si. In other words, the BE of S$_1$ in the ML film should be similar to the BE of the component in the BG$_o$ layer that is bonded to Si in the interface. At the same time, the component that binds to Si in both the BG$_o$ and BG$_{ML}$ must be approximately the same Z distance from the top Si layer. A comparison of the BG$_o$ and BG$_{ML}$+ML film data in Table I and the red dashed line in Fig. 7 shows that only the S$_1$ peak in the 5-component C 1s spectrum meets both these combined requirements. Based on these observations, we propose that the 5-component fit to the BG$_o$ layer's XPS data represents the actual C 1s spectra and that the previous Emtsev *et al.* [1] interpretation correctly assigns S$_1$ as being the BG$_o$ carbon component bonded to Si. The incorrect assignment of the bonding species in the prior XSW analysis was most likely due to the XPS signal being a mixture of two different spectra from ML and buffer layer partial coverages.

The XSW-derived distance between the S$_1$ carbon in the BG$_o$ layer and the top Si layer is 2.26 Å, comparable to the 2.1(1) Å distance measured in previous XSW work [18] but larger that the 1.9 Å bond length measured by STEM [32]. The differences between the XSW results and STEM values is likely due to assigning the Si top layer Z position as the zero of the Z scale based solely on the value derived from the Si 2s XSW yield. Since the Si 2s yield contains contributions from several bilayers, which we will show have different Z distributions, the XSW-derived Si position will have systematic errors.

Finally, even though the 5-component fit gives the best overall density profile, there are problems. The density profile is not as sharp as STEM results would have predicted. Furthermore, we expect from the model in Fig. 3 that there should be significantly more S$_2$ carbon compared to S$_1$. The XSW results in Table II give nearly the same concentrations for both S$_1$ and S$_2$. We believe these problems with the XSW results are associated with the difficulty of accurately deconvoluting the closely spaced C 1s components in the XPS spectra. To improve on the XSW structural result we must combine these findings with our XRR results of the BG$_o$ and BG$_{ML}$+ML films.

C. Surface x-ray diffraction

To fit the x-ray data, we use four SiC bilayers above the bulk with a buffer graphene layer above (see Fig. 1). We also allow up to two partial graphene layers above the buffer. The scattered x-ray intensity $I(\Theta,\ell)$ is then

$$I(\Theta,\ell) = A(\Theta,\ell)e^{-4\gamma_{\mathrm{SiC}}\sin^2\pi\ell/2}\left|\frac{F_{\mathrm{bulk}}(\ell)}{1-e^{-2\pi i\ell}} + F_I(\ell) + \frac{\rho_{\mathrm{G}}}{\rho_{\mathrm{SiC}}}[F_{\mathrm{BG}}(\ell)+F_{\mathrm{G}}(\ell)]\right|^2, \qquad (3)$$

where F_{bulk} is the bulk $4H$-SiC structure factor [39], modified by the crystal truncation term, $(1-e^{-2\pi i\ell})^{-1}$ (see Ref. [40]), F_I is the structure factor of the 4-bilayer SiC interface region, F_{BG} is the buffer graphene structure factor, and F_{G} is the structure factor of any ML graphene layers above the buffer. $F_{\mathrm{BG}}(\ell)$ and $F_{\mathrm{G}}(\ell)$ in Eq. (3) are weighted by the ratio of the areal atomic densities of a $4H$-SiC(0001) bilayer and a graphene (0001) plane: $\rho_{\mathrm{G}}/\rho_{\mathrm{Si}} = 3.132$. The factor properly normalizes the scattered amplitude from the graphene layer per $4H$-SiC(0001) (1×1) unit cell. $A(\Theta,\ell)$ is a term that contains all corrections due to the experimental geometry [25,41,42]. The exponential term accounts for the substrate roughness caused by half-cell step fluctuations in the SiC surface (the predominant step height on $4H$ samples [15]: $c_{\mathrm{SiC}}/2$). γ_{SiC} is the variance in the number of half-cell layers in the surface due to steps [43]. Roughly, γ_{SiC} is proportional to the SiC step density.

$F_I(\ell)$ in Eq. (3) is the structure factor of the top four SiC C-Si bilayers plus an additional layer of Si to allow for the possibility of Si adatoms or a relaxed Si layer bonded to the buffer graphene (see Fig. 1). The interface structure factor is then

$$F_I(\ell) = \sum_{j=1}^{9} f_j(\ell)\rho_j e^{-\sigma_j^2(2\pi\ell/c_{\mathrm{SiC}})^2/2}e^{i2\pi\ell z_j/c_{\mathrm{SiC}}}, \qquad (4)$$

where ρ_j is the relative atom density for the jth interface layer at a vertical position z_j ($\rho_j = 1$ for a bulk layer corresponding to 8.22×10^{-16} atoms/cm^2). It was found that the additional Si layer was not needed to fit the experimental reflectivity and will not be discussed in Sec. IV. The zero height is chosen as the top layer of Si atoms in the top SiC bilayer. $f_j(\ell)$ is the atomic form factor of C or Si depending on the layer. A normalized Gaussian of width σ_j has been convoluted with each layer to include possible layer disorder [similarly to Eq. (2b), used to describe the XSW vertical distribution].

To be consistent with the XSW results, we allow the buffer to be composed of n distinct carbon layers. The multilayer graphene structure factor can then be written in a general form similar to Eq. (4):

$$F_{\mathrm{BG}}(\ell) = f_{\mathrm{C}}(\ell)P_{\mathrm{BG}}\sum_{s=1}^{n}\theta_s e^{-\sigma_s^2(2\pi\ell/c_{\mathrm{SiC}})^2/2}e^{2\pi i l z_s/c_{\mathrm{SiC}}}, \qquad (5)$$

where f_{C} is the atomic form factor for carbon, P_{BG} is the areal coverage of buffer graphene, and θ_s is the fractional coverage of each component in the buffer such that $\Sigma\theta_s = 1$.

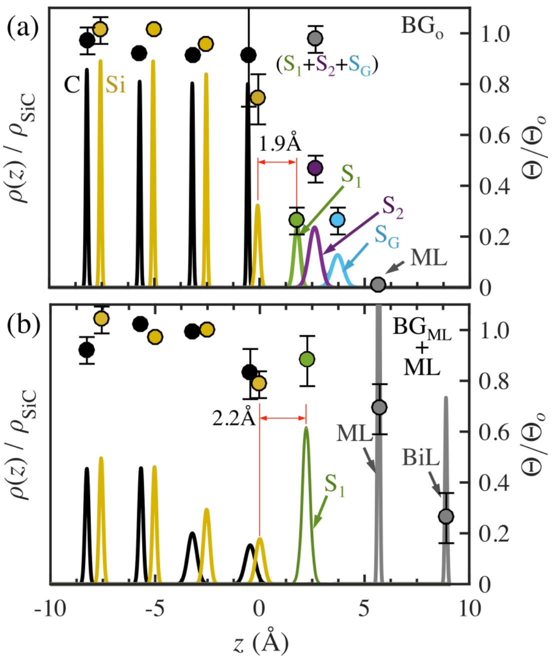

FIG. 8. The XRR-derived vertical density profiles, $\rho(z)$, for both (a) the BG$_o$ and (b) the BG$_{\mathrm{ML}}$+ML films. Densities are normalized to the bulk SiC density. Solid lines are the density profiles (left axis) for SiC Si (yellow) and C atoms (black), for buffer S$_1$ (green), S$_2$ (purple), and S$_G$ (cyan) carbon species, and for ML or bilayer graphene, BiL (gray). Circles represent the integrated layer coverages, θ, of each layer or component (right scale). θ for the bulk components are relative to the SiC in-plane density while the buffer and ML θs are relative to a ML graphene density.

The structure factor of graphene above the buffer layer is

$$F_{\mathrm{G}}(\ell) = f_{\mathrm{C}}(\ell)\sum_{m=1}^{M}P_m e^{-\sigma_m^2(2\pi\ell/c_{\mathrm{SiC}})^2/2}e^{2\pi i l z_m/c_{\mathrm{SiC}}}, \qquad (6)$$

where P_m is the coverage of the mth graphene layer.

To fit the experimental reflectivity to Eq. (3), we use a lasso fitting routine [44]. The lasso technique allows us to use the XSW-derived buffer and known SiC bulk parameters as starting points (default parameters). Changes in these parameters are penalized in the ordinary least-squares regression (OLS). The penalties are initially set to be very large to identify which parameters in Eq. (3) give the largest reduction in the OLS χ^2. Gradually, all penalties are reduced and new default parameters are updated until the model has converged to the minimized χ^2 defined by Ref. [45] (see Supplemental Material [30]) [46]. This enables a seamless connection of the XSW-derived parameters with the XRR parameters, placing the results of both techniques on an equal footing.

IV. DISCUSSION

Figure 8 shows a comparison of the density profiles from the buffer BG$_o$ and BG$_{\mathrm{ML}}$+ML films derived from the XRR fits in Fig. 4. The fit parameters are given in Table IV. The calculated reflectivity for a buffer BG$_o$ film starts with the S$_1$, S$_2$, and S$_G$ positions and widths derived from the XSW parameters. Fits starting with only S$_1$ and S$_2$ always have an

TABLE IV. Comparison of the BG_o and BG_{ML} structural parameters from both XRR and the 5-component XSW analysis. $\Delta_{\text{Si-C}}$ is the C-Si vertical separation in the top SiC bilayer (see Fig. 1). $\Delta_{\text{Si-C}}$ for the top bilayer is measured directly in XRR, but represents a more bulklike value in XSW results.

		$Z - Z_{\text{Si}}$ (Å)			σ (Å)			θ (ML_G)			Interface layer		
											$\Delta_{\text{Si-C}}$	θ (ML_{SiC})	
		S_1	S_2	S_G	S_1	S_2	S_G	S_1	S_2	S_G	(Å)	Si	C
BG_o	XRR	1.9(1)	2.7(1)	3.8(1)	0.15(5)	0.27(2)	0.3(1)	0.26(6)	0.47(6)	0.26(4)	0.47(2)	0.75(10)	0.9(2)
	XSW	2.26(3)	2.5(1)	3.13(6)	0.36(4)	0.48(7)	0.3(1)	0.33(1)	0.32(1)	0.36(2)	0.69(2)		
BG_{ML}	XRR	2.22(7)			0.2(1)			0.9(1)			0.46(5)	0.79(5)	0.8(1)
	XSW	2.30(5)			0.52(3)						0.33(2)		

order of magnitude higher χ^2 values and will not be discussed here [46]. The higher χ^2 values, using only two carbon layers in the buffer, support our early argument that a 5-component fit to the C 1*s* spectrum is necessary to get the correct vertical position of S_1 and S_2 from the XSW analysis. The ML film uses a single component for the BG_{ML} film as determined from the preceding XSW analysis. Note that the XRR-determined ML coverage is less than 1% for the BG_o film [see Fig. 8(a)], consistent with the Raman ML estimate in Fig. 2. In the ML sample, there is a significant bilayer (BiL) graphene coverage (27%) in Fig. 8(b).

Like the XSW profiles, the XRR analysis shows that the BG_o layer distribution is very broad compared to the BG_{ML} layer in the ML film. Associated with the change in the buffer's *Z* width, we find that the buffer-Si distance gets larger by 0.3 Å when a ML has grown above it. This vertical change in distance results in a physically reasonable volume conservation when one also considers the previously observed transition from the larger in-plane incommensurate lattice spacing of BG_o to the smaller commensurate lattice in the case of BG_{ML} [9]. It apparently occurs concomitantly with a change in the distribution of buffer-Si bonds at the interface. Both the change in width and bond distance are consistent with ARPES measurements that show a change in the band structure of the buffer when a ML grows above it [9].

The XRR analysis finds that the bonding component S_1 in the BG_o layer is 1.9 Å above the top Si layer, the same distance measured by STEM [32]. The distance between the buffer S_1 carbon and the last Si layer is essentially the same as the bulk Si-C bond (1.89 Å) confirming that the bond between S_1 carbon and substrate Si has a significant covalent component [18,32]. We note that the XRR-derived distance for S_1 is about 17% closer to the interface than the XSW result. As discussed in Sec. III B this small difference is not unusual given that the top Si-layer position is determined from the XSW yield of the Si 2*s* spectrum that has a significant contribution from deeper bulklike bilayers with different vertical relaxations. Indeed, while the XSW analysis gives the C-Si separation in the top SiC bilayer as 0.69 Å, nearly the bulk value (0.63 Å), the XRR analysis finds that the C-Si separation has relaxed to be nearly 30% shorter (0.47 Å) than in the bulk (see Table IV).

The XRR-derived vertical density profile of the BG_o layer is both sharper and wider than the XSW distribution. Figure 9 shows a comparison of the XRR and XSW derived distributions. We believe the broader XSW distribution is due to a combination of chemical selectivity and problems with the fitting of the C 1*s* spectrum. For instance, carbon with the same BE can be at two different positions. In XSW analysis, where we assume a Gaussian distribution for all carbon with the same BE [see Eq. (2)], the yield curve fitting would give a single broad Gaussian density profile. XRR on the other hand would give two well separated Gaussians, since it only depends on the physical location of the carbon, not its chemical bonding. While in principle the XSW analysis could include a more complicated density distribution in Eq. (1), the difficulty in fitting the C 1*s* spectrum discussed in Sec. III A precludes us from making strong claims about the XSW-derived density profiles.

The XRR-determined BG_o layer width is 2.4(4) Å compared to 1.5(2) Å (including σs) found in the XSW analysis. We point out that both our XRR and XSW BG_o widths are much wider than the previous XSW results of Emery *et al.* [18] (FWHM = 0.9 Å). The difference is not unexpected because the prior XSW results were from multilayer graphene films with a large areal coverage of BG_{ML} buffer and a much smaller coverage of BG_o buffer. Based on our ML results, the early UHV films, which were composed of primarily ML graphene with little BG_o buffer [18], would have measured a buffer width that was a weighted average of a majority BG_{ML} film with width 0.4(1) Å and a minority contribution from the broad BG_o film with width 2.4(4) Å. Assuming an 80%

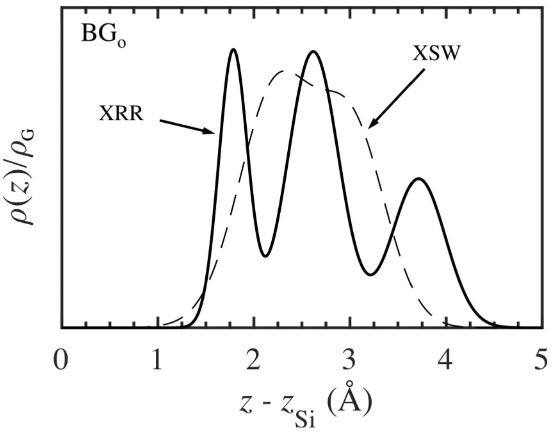

FIG. 9. A comparison of the BG_o layer's vertical density distribution, $\rho(z)$, derived from XSW (dashed line) and XRR (solid line). The density is normalized to the density of a graphene layer.

ML film, an average buffer width of 0.8 Å would have been measured, close to the 0.9 Å that was measured in Ref. [18].

While we find a wide $\mathrm{BG_o}$ layer, it is not unprecedented. Large vertical buffer layer widths have also been suggested by scanning tunneling microscopy (STM) measurements. Chen *et al.* [47] argue that large amplitude height variations in the (6×6) buffer structure, seen in both filled and empty state images, are topographical. They find vertical oscillations between 1.5 Å and 3.2 Å. The larger widths were observed in films that were annealed for longer times, implying that they are associated with more ordered buffer films. However, similar oscillations seen by Riedl *et al.* [17] were interpreted as being partially due to electronic effects so it remains difficult to make direct comparisons of our $\mathrm{BG_o}$ layer width with STM-measured corrugations. *Ab initio* calculations, using a bulk-terminated SiC surface, predict a significant $\mathrm{BG_o}$ layer modulation of 1.2 Å [8]. As we now discuss, the interface is far from bulk terminated and could induce much larger theoretical modulations if a more realistic SiC interface structure were used.

The structure of the SiC interface layer and how Si in this layer is bonded to buffer carbon are the most important questions about this system. The reflectivity shows that while the last Si layer remains relatively sharp, its density is only 75% of its bulk value (i.e., 20% Si vacancies) (see Table IV). A similar Si vacancy concentration was reported in previous XRR studies using UHV-grown samples and was presumed to be due to a growth artifact [18]. Our results strongly suggest that the depleted top Si layer is in fact an equilibrium structure. We say this because the depleted fraction in the top Si layer is independent of the growth method. The Si vacancy concentration in our high-temperature, high Si vapor pressure environment is the same as the concentration found in the prior low-temperature, low Si vapor pressure UHV environment [18]. Furthermore, the Si vacancy concentration is the same in both the $\mathrm{BG_o}$ and $\mathrm{BG_{ML}}$+ML films (see Table IV) even though the ML grows at a temperature 150 °C higher than the $\mathrm{BG_o}$ layer. All of these results point to the depleted top Si layer being an equilibrium structure that is relatively independent of temperature and Si vapor pressure. The idea that Si vacancies may exist in the buffer-SiC system has been explored theoretically. Calculations have shown that Si vacancies or C interstitials in the interface layer below the $\mathrm{BG_o}$ layer lead to lower total surface energies that can give rise to a number of possible large $\mathrm{BG_o}$ corrugations [48].

Besides the high Si vacancy concentration, there is a significant change in the carbon-silicon spacing in the top SiC bilayer. The C-Si Z spacing, $\Delta_{\text{Si-C}}$, in the SiC bilayer below $\mathrm{BG_o}$ is 30% shorter compared to a bulk SiC bilayer and half the distance predicted by *ab initio* calculations in a bulk-terminated surface with a $\mathrm{BG_{ML}}$+ML film [12]. It is likely that the vacancies in the top SiC bilayer lead to the additional bulk peak $\mathrm{C'_B}$ in the 5-component C 1s spectra in Figs. 5(b) and 5(c) (see Supplemental Material [30]). We suggest that not only are Si vacancies a part of the equilibrium SiC-buffer system but that they most likely drive the incommensurate buffer-SiC structure recently found in surface x-ray diffraction studies [9]. We expect that future theoretical work will support this assertion.

We point out that while the XSW analysis finds that there is equal $\mathrm{S_2}$ and $\mathrm{S_1}$ carbon (see Table IV), the XRR-derived coverages find that there are nearly twice as many $\mathrm{S_2}$ carbon atoms compared to $\mathrm{S_1}$. The higher $\mathrm{S_2}$ coverage is more constant with the model in Fig. 3 that would suggest approximately a 3:1 ratio of $\mathrm{S_2}$ to $\mathrm{S_1}$. Since the $\mathrm{S_1}$ bonding component, derived from the XRR, makes up 26% of the carbon in the $\mathrm{BG_o}$ layer (see Table IV), the $\mathrm{S_1}$ coverage must put an upper limit on the number of Si-graphene bonds in the buffer layer. If each $\mathrm{S_1}$ carbon atom bonds with a single Si atom in the top SiC interface layer, the reflectivity would estimate that 81% of the interfacial Si is bonded to the buffer layer. Of course it is not only the number of bonds that determine the $\mathrm{BG_o}$'s electronic structure, but how these bonds are distributed. *Ab initio* calculations of the $\mathrm{BG_o}$ layer find that 25% of the buffer carbon is bonded to 78% of the Si in the top layer assuming a bulk-terminated surface [7]. Tight-binding calculations using an incommensurate distortion of the bulk surface predict a much lower number of bonded buffer carbon (15%) [9]. It is very likely that allowing Si vacancies in the top SiC layer will lead to an opening of a gap in the band structure of buffer graphene in *ab initio* models.

Finally, a comparison of Figs. 8(a) and 8(b) reveals that, with the exception of the last Si layer, the widths of the interface C and Si remain relatively well ordered after the buffer has formed ($\sigma_{\mathrm{C}} = 0.12$ Å and $\sigma_{\mathrm{Si}} = 0.05$ Å). Once the ML is grown at a higher temperature, there is considerably more vertical disorder in the interface. In the last two SiC bilayers, the C widths double compared to the buffer-only interface and the Si width in the second bilayer triples. The increased vertical disorder is consistent with an increase in the in-plane disorder of the interface and an increase in the $\mathrm{BG_{ML}}$ in-plane strain when the ML grows [9]. Since the ML is grown 150 °C higher than the buffer-only film, entropic disorder in the SiC below the ML film may become important. This suggests that annealing studies (at temperatures less than the ML growth temperature) will need to be carried out to see whether the interface order can be further improved.

V. CONCLUSION

In this work, we have studied the structure of the first graphene layer that grows on SiC(0001) (known as "buffer" graphene). By using samples with highly uniform and controlled graphene coverages, we are able to show that the buffer's structure is dramatically altered when monolayer graphene is grown above it. These results correlate well with electronic changes that occur with ML growth. From essentially ML free samples, we are able to clear up inconsistencies in early works as to which component in the buffer's C 1s spectrum is associated with carbon bonded to Si in the SiC interface. We show that the $\mathrm{S_1}$ peak at a binding energy of 285.2 eV is from buffer carbon sp^3-bonded to Si.

One of the most important findings of this work is that the SiC interface below the buffer graphene cannot be bulk terminated. Instead we show that the last Si layer in the SiC interface is substantially reconstructed. By comparing samples grown under different growth conditions, we show that the top Si bilayer in the interface has a large equilibrium concentration of Si vacancies (20% of the bulk value). The effect of the reduced number of Si atoms is to decrease the top SiC bilayer distance by 30% of the bulk value. This planarization of the SiC bilayer may explain why the SiC interfacial layer, along with the buffer layer, becomes incommensurate with the bulk SiC. We also find that less than 26% of the BG_0 buffer layer carbon is bonded to the substrate. While the exact density of Si in the top layer cannot be determined, we can report that the number of Si atoms bonded to the buffer carbon can be no more than 55% of the Si atoms in the top SiC bilayer. We believe these results will act as a new starting SiC interfacial structure for future *ab initio* calculations that will help us to understand the semiconducting properties of this graphene film.

We also show that the vertical corrugation of the buffer layer is very large, $\Delta z = 2.4(4)$ Å, and that the buffer's width reduces to $\Delta z = 0.4(1)$ Å when a monolayer grows above the buffer. The reduction in the buffer's width is associated with a slight increase in the Si-buffer carbon bond length. Finally, we find that the SiC interface becomes more vertically disordered when the monolayer forms. This correlates with previous x-ray diffraction results that find an increase in the buffer's in-plane disorder when a monolayer forms above it [9]. This is most likely due entropic disorder at the higher growth temperature of the monolayer and the decrease of Si out-diffusion caused by the buffer carbon film. The results suggest that annealing may improve the interface order.

ACKNOWLEDGMENTS

This research was supported by the National Science Foundation under Grant No. DMR-1401193. P.F.M. also acknowledges support from the NSF under Grant No. DGE-1069091. Additional support came from the Partner University Fund from the French Embassy. The authors would like to thank W. de Heer for use of the Keck Lab facilities. Finally, we wish to acknowledge the staff and technical support given for this project by the Synchrotron Soleil under Projects No. 20150681 and No. 20150682.

[1] K. V. Emtsev, F. Speck, T. Seyller, L. Ley, and J. D. Riley, Phys. Rev. B **77**, 155303 (2008).

[2] M. S. Nevius, M. Conrad, F. Wang, A. Celis, M. N. Nair, A. Taleb-Ibrahimi, A. Tejeda, and E. H. Conrad, Phys. Rev. Lett. **115**, 136802 (2015).

[3] A. L. Walter, H. Sahin, J. Kang, K.-J. Jeon, A. Bostwick, S. Horzum, L. Moreschini, Y. J. Chang, F. M. Peeters, K. Horn, and E. Rotenberg, Phys. Rev. B **93**, 075439 (2016).

[4] C. Riedl, C. Coletti, T. Iwasaki, A. A. Zakharov, and U. Starke, Phys. Rev. Lett. **103**, 246804 (2009).

[5] A. Mattausch and O. Pankratov, Phys. Rev. Lett. **99**, 076802 (2007).

[6] F. Varchon, R. Feng, J. Hass, X. Li, B. N. Nguyen, C. Naud, P. Mallet, J.-Y. Veuillen, C. Berger, E. H. Conrad, and L. Magaud, Phys. Rev. Lett. **99**, 126805 (2007).

[7] S. Kim, J. Ihm, H. J. Choi, and Y.-W. Son, Phys. Rev. Lett. **100**, 176802 (2008).

[8] F. Varchon, P. Mallet, J.-Y. Veuillen, and L. Magaud, Phys. Rev. B **77**, 235412 (2008).

[9] M. Conrad, F. Wang, M. Nevius, K. Jinkins, A. Celis, M. N. Nair, A. Taleb-Ibrahimi, A. Tejeda, Y. Garreau, A. Vlad, A. Coati, P. F. Miceli, and E. H. Conrad, Nano Lett. **17**, 341 (2017).

[10] A. J. V. Bommel, J. E. Crombeen, and A. V. Tooren, Surf. Sci. **48**, 463 (1975).

[11] I. Forbeaux, J.-M. Themlin, and J.-M. Debever, Phys. Rev. B **58**, 16396 (1998).

[12] J. Sforzini, L. Nemec, T. Denig, B. Stadtmüller, T.-L. Lee, C. Kumpf, S. Soubatch, U. Starke, P. Rinke, V. Blum, F. C. Bocquet, and F. S. Tautz, Phys. Rev. Lett. **114**, 106804 (2015).

[13] J. Hass, W. A. de Heer, and E. H. Conrad, J. Phys.: Condens. Matter **20**, 323202 (2008).

[14] A. Charrier, A. Coati, T. Argunova, F. Thibaudau, Y. Garreau, R. Pinchaux, I. Forbeaux, J.-M. Debever, M. Sauvage-Simkin, and J.-M. Themlin, J. Appl. Phys. **92**, 2479 (2002).

[15] J. Hass, R. Feng, T. Li, X. Li, Z. Zong, W. A. de Heer, P. N. First, E. H. Conrad, C. A. Jeffrey, and C. Berger, Appl. Phys. Lett. **89**, 143106 (2006).

[16] X. Gao, S. Chen, T. Liu, W. Chen, A. T. S. Wee, T. Nomoto, S. Yagi, K. Soda, and J. Yuhara, Phys. Rev. B **78**, 201404 (2008).

[17] C. Riedl, U. Starke, J. Bernhardt, M. Franke, and K. Heinz, Phys. Rev. B **76**, 245406 (2007).

[18] J. D. Emery, B. Detlefs, H. J. Karmel, L. O. Nyakiti, D. K. Gaskill, M. C. Hersam, J. Zegenhagen, and M. J. Bedzyk, Phys. Rev. Lett. **111**, 215501 (2013).

[19] W. A. de Heer, C. Berger, M. Ruan, M. Sprinkle, X. Li, Y. Hu, B. Zhang, J. Hankinson, and E. Conrad, Proc. Natl. Acad. Sci. USA **108**, 16900 (2011).

[20] M. S. Nevius, Improved growth, ordering, and characterization of sidewall epitaxial graphene nanoribbons, Ph.D. thesis, Georgia Institute of Technology, 2016.

[21] F. Fromm, P. Wehrfritz, M. Hundhausen, and T. Seyller, New J. Phys. **15**, 113006 (2013).

[22] J. Palmer, J. Kunc, Y. Hu, J. Hankinson, Z. Guo, C. Berger, and W. A. de Heer, Appl. Phys. Lett. **105**, 023106 (2014).

[23] K. V. Emtsev, A. Bostwick, K. Horn, J. Jobst, G. L. Kellogg, L. Ley, J. L. McChesney, T. Ohta, S. A. Reshanov, J. Rohrl, E. Rotenberg, A. K. Schmid, D. Waldmann, H. B. Weber, and T. Seyller, Nat. Mater. **8**, 203 (2009).

[24] J. Kunc, Y. Hu, J. Palmer, C. Berger, and W. A. de Heer, Appl. Phys. Lett. **103**, 201911 (2013).

[25] E. Vlieg, J. Appl. Crystallogr. **30**, 532 (1997).

[26] J. Zegenhagen, Surf. Sci. Rep. **18**, 202 (1993).

[27] M. J. Bedzyk, in *Encyclopedia of Condensed Matter Physics*, edited by G. J. Bassani, F. Liedl, and P. Wyder (Elsevier, Oxford, 2005), Vol. 6, pp. 330–341.

[28] J.-P. Rueff, J. M. Ablett, D. Colin, D. Prieur, T. Moreno, V. Baldent, B. Lassalle-Kaiser, J. E. Rault, M. Simon, and A. Shukla, J. Synchrotron Radiat. **22**, 175 (2015).

[29] Y. Takata, Y. Kayanuma, M. Yabashi, K. Tamasaku, Y. Nishino, D. Miwa, Y. Harada, K. Horiba, S. Shin, S. Tanaka, E. Ikenaga, K. Kobayashi, Y. Senba, H. Ohashi, and T. Ishikawa, Phys. Rev. B **75**, 233404 (2007).

[30] See Supplemental Material at http://link.aps.org/supplemental/10.1103/PhysRevB.96.195304 for the C 1*s* core level fit procedure and how the statistical relevance of the multi-peak fits were evaluated. This includes a complete list of fit parameters, instrument resolution determination, and other instrument effects. The Supplement also includes calculation of the phase and reflectivity of the (004) standing wave and a complete description of the lasso regression techniques used for fitting the XRR.

[31] P. J. Brown, A. G. Fox, E. N. Maslen, M. A. O'Keefe, and B. T. M. Willis, *Graphene: Properties, Preparation, Characterisation and Devices* (Elsevier, Oxford, 2014).

[32] M. N. Nair, I. Palacio, A. Celis, A. Zobelli, A. Gloter, S. Kubsky, J.-P. Turmaud, M. Conrad, C. Berger, W. de Heer, E. H. Conrad, A. Taleb-Ibrahimi, and A. Tejeda, Nano Lett. **17**, 2681 (2017).

[33] I. Robinson and E. Vlieg, Surf. Sci. **261**, 123 (1992).

[34] I. A. Vartanyants and J. Zegenhagen, Solid State Commun. **113**, 299 (1999).

[35] P. J. Brown, A. G. Fox, E. N. Maslen, M. A. O'Keefe, and B. T. M. Willis, in *International Tables for Crystallography, Vol. C, Mathematical, Physical, and Chemical Tables*, edited by E. Prince (Springer, Netherlands, Dordrecht, 2004), pp. 554–595.

[36] D. T. Cromer, J. Appl. Crystallogr. **16**, 437 (1983).

[37] D. P. Woodruff, Rep. Prog. Phys. **68**, 743 (2005).

[38] A. Authier, in *International Tables for Crystallography, Vol. B, Reciprocal Space*, edited by U. Shmueli (Springer, Netherlands, Dordrecht, 2001), pp. 534–551.

[39] A. Bauer, P. Reischauer, J. Kräusslich, N. Schell, W. Matz, and K. Goetz, Acta Crystallogr., Sect. A **57**, 60 (2001).

[40] I. K. Robinson, Phys. Rev. B **33**, 3830 (1986).

[41] I. Robinson, in *Handbook on Synchrotron Radiation*, edited by G. Brown and D. Moncton (North-Holland, Amsterdam, 1991), Vol. 3, pp. 221–266.

[42] R. Feng, Structural and kinetics study of quantum size effect Pb islands grown on Si(111), Ph.D. thesis, Georgia Institute of Technology, 2006.

[43] W. Elliott, P. Miceli, T. Tse, and P. Stephens, Phys. B (Amsterdam) **221**, 65 (1996).

[44] R. Tibshirani, J. Roy. Stat. Soc. Ser. B (Methodological) **58**, 267 (1996).

[45] I. K. Robinson and D. J. Tweet, Rep. Prog. Phys. **55**, 599 (1992).

[46] M. D. Conrad, Structure and properties of incommensurate and commensurate phases of graphene on SiC(0001), Ph.D. thesis, Georgia Institute of Technology, 2017.

[47] W. Chen, H. Xu, L. Liu, X. Gao, D. Qi, G. Peng, S. C. Tan, Y. Feng, K. P. Loh, and A. T. S. Wee, Surf. Sci. **596**, 176 (2005).

[48] H. Kageshima, H. Hibino, H. Yamaguchi, and M. Nagase, Jpn. J. Appl. Phys. **50**, 095601 (2011).